

In-situ monitoring of melt pool images for porosity prediction in directed energy deposition processes

Mojtaba Khanzadeh, Sudipta Chowdhury, Mark A. Tschopp, Haley R. Doude,
Mohammad Marufuzzaman & Linkan Bian

To cite this article: Mojtaba Khanzadeh, Sudipta Chowdhury, Mark A. Tschopp, Haley R. Doude, Mohammad Marufuzzaman & Linkan Bian (2019) *In-situ* monitoring of melt pool images for porosity prediction in directed energy deposition processes, IJSE Transactions, 51:5, 437-455, DOI: 10.1080/24725854.2017.1417656

To link to this article: <https://doi.org/10.1080/24725854.2017.1417656>



Accepted author version posted online: 14 Dec 2017.
Published online: 13 Mar 2018.



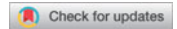
Submit your article to this journal



Article views: 1088

[View related articles](#) View Crossmark data 

Citing articles: 15 View citing articles



In-situ monitoring of melt pool images for porosity prediction in directed energy deposition processes

Mojtaba Khanzadeh^a, Sudipta Chowdhury^a, Mark A. Tschopp^b, Haley R. Doude^c, Mohammad Marufuzzaman^a and Linkan Bian^{a,c}

^aDepartment of Industrial and Systems Engineering, Mississippi State University, Starkville, MS, USA; ^bArmy Research Laboratory, Aberdeen Proving Ground, MD, USA; ^cCenter for Advanced Vehicular Systems (CAVS), Mississippi State University, Starkville, MS, USA

ABSTRACT

One major challenge of implementing Directed Energy Deposition (DED) Additive Manufacturing (AM) for production is the lack of understanding of its underlying process–structure–property relationship. Parts manufactured using the DED technologies may be too inconsistent and unreliable to meet the stringent requirements for many industrial applications. The objective of this research is to characterize the underlying thermo-physical dynamics of the DED process, captured by melt pool signals, and predict porosity during the build. Herein we propose a novel porosity prediction method based on the temperature distribution of the top surface of the melt pool as an AM part is being built. Self-Organizing Maps (SOMs) are then used to further analyze the two-dimensional melt pool image streams to identify similar and dissimilar melt pools. X-ray tomography is used to experimentally locate porosity within the Ti-6Al-4V thin-wall specimen, which is then compared with predicted porosity locations based on the melt pool analysis. Results show that the proposed method based on the temperature distribution of the melt pool is able to predict the location of porosity almost 96% of the time when the appropriate SOM model using a thermal profile is selected. Results are also compared with a previous study, that focuses only on the shape and size of the melt pool. We find that the incorporation of thermal distribution significantly improves the accuracy of porosity prediction. The significance of the proposed methodology based on the melt pool profiles is that this can lead the way toward *in situ* monitoring and minimize or even eliminate pores within the AM parts.

ARTICLE HISTORY

Received 12 May 2017
Accepted 5 December 2017

KEYWORDS

Additive manufacturing;
porosity; clustering; *in situ*
monitoring; melt pool

1. Introduction

Our objective is to develop an *in situ* signal processing methodology for characterizing the thermo-physical dynamics of Directed Energy Deposition (DED) melt pool signals, which can be subsequently used to predict process anomalies during the build. Metallic Additive Manufacturing (AM) parts are now used as functional parts within many industrial sectors such as tooling, dental, medical, and aerospace. This popularity is driven by virtue of its unique feature of generating complex-shaped, functionally graded, or custom-tailored parts that can be utilized for a variety of engineering and industrial applications (Thompson *et al.*, 2015). According to the most recent Wohlers' report, the sale of AM systems and corresponding services is projected to reach 5.5 billion USD by the year 2019 (Wohlers, 2016). Although AM has experienced tremendous growth and success in non-structural applications, variations in the quality and mechanical properties of AM parts, due to the presence of defects, can limit its use in load-bearing or mission-critical applications. *Mission-critical application* refers to the applications of manufactured parts where tough performance standards and requirements must be fulfilled before they can be used in the real world.

The existence of porosity is a major quality issue for AM parts. A few of the hypothesized causes of porosity in parts

are the rapid solidification of AM parts, entrapped gas, incomplete powder melting, and lack of fusion (Shamsaei *et al.*, 2015; Thompson *et al.*, 2015). The existing approaches for porosity detection are based on X-ray Computed Tomography (CT), ultrasonic scanning, and other post-manufacturing characterization, which can be expensive and time-consuming. Therefore, the next-generation AM monitoring/control system needs the capability for *in situ* monitoring and prediction of process defects via analysis of process signals (Seifi *et al.*, 2016).

The melt pool, or molten pool, is the region of superheated molten metal in proximity to the laser/material interface; typically it has the form of a spherically shaped droplet that moves at the traverse speed (Thompson *et al.*, 2015). Melt pool is the initiation of the solidified part, and its morphology and thermal distribution are eminent indicators of the fabricated part's microstructure and thus final quality. Figure 1 demonstrates the potential relationship between characteristics of melt pool images and porosity, based on experimental data generated by the Additive Manufacturing Laboratory at Mississippi State University.

When the thermal distribution of melt pools exhibits abnormal behaviors, various types of pores may be generated. Melt pool behaviors are directly related to the formation of porosity

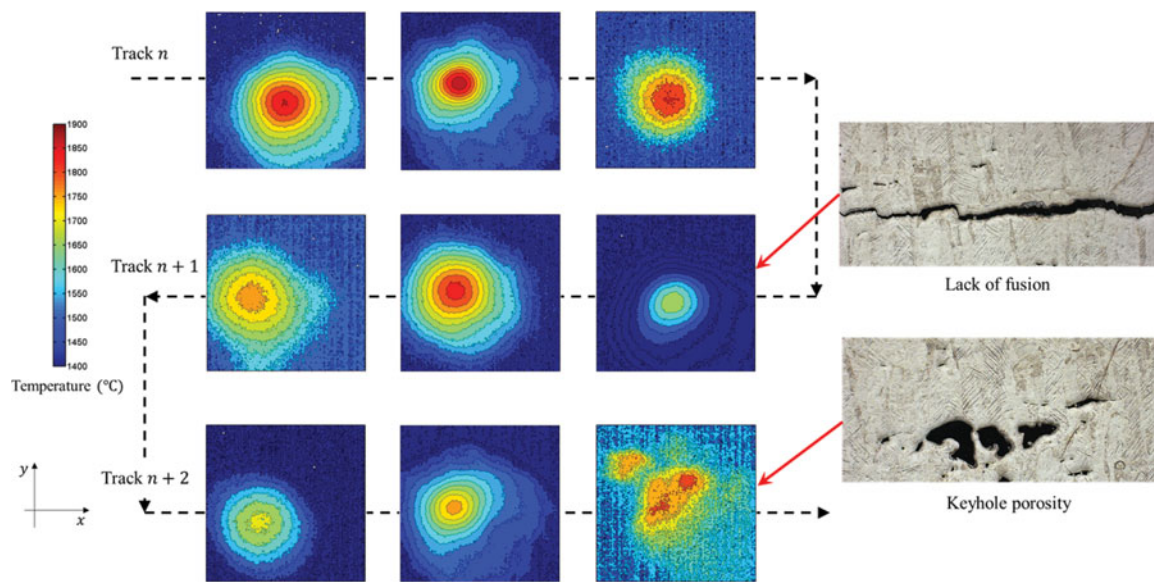


Figure 1. Relationship between melt pool characteristics and porosity. The image colors represent the temperature of the melt pool ($^{\circ}\text{C}$).

in the parts. For instance, the fundamental origin of lack-of-fusion porosity is caused by insufficient overlap of successive melt pools. Moreover, the keyhole effect results from generating a deep V-shaped melt pool and vaporizing elements within the melt pool, which can cause gas/vapor to get trapped as porosity within the material. Once the melt pool behaviors are correlated to the porosity of the fabricated parts, control/correction actions can be taken to reduce porosity during the build. Extracting the melt pool characteristics and correlating the extracted features to microstructure anomalies will lead to real-time, non-destructive detection of part defects. Most of the existing studies for modeling the time-varying melt pool can be broadly categorized into two groups: (i) characterizing the melt pool based on the morphological characteristics and (ii) capturing the melt pool's thermal characteristics. The former group of studies focuses on capturing the changes in the size, length, depth, area, and other geometric features of the melt pools during the build (see Pinkerton and Lin (2004) and Qi *et al.* (2006)), whereas the latter focuses on the temperature measurements over the melt pool, such as peak temperature, average temperature, etc. (see Tang and Landers (2010) and Chandrasekhar *et al.* (2015)). Most of these methods were developed based on physics-based differential equations that govern the underlying thermo-physical process (Picasso and Hoadley, 1994; Kim and Peng, 2000). However, such methods may not accurately capture the uncertainty associated with the process, and the resulting simulated thermal history tends to deviate from reality (Tang *et al.*, 2009).

There is an urgent need to develop an efficient methodology for extracting features based on thermal imaging data streams during the actual build of the parts that can be used to signal the formation of porosity. We propose an imaging processing method, based on functional data analysis, to characterize the thermal distribution of the top surface of the melt pool. Note that characterization of the melt pool signals is challenging, due to large data volume, low signal-to-noise ratio, ill-structured data (e.g., different melt pools varying in sizes), and missing data measurements. To address these challenges, we apply

a spherical transformation and convert melt pool thermal distributions with different sizes/shapes to temperature measurements with identical support in the spherical domain. The reason for using a spherical transformation of the data instead of other transformations is that the position of the melt pool in our study is specified by three numbers, the radial distance of that point from a fixed origin that denotes its temperature and its polar and azimuth angles that define the pixels of melt pool images. Hence, spherical transformation is a suitable option for the authors to convert the melt pool thermal distributions with different sizes/shapes to temperature measurements with identical support in the spherical domain. Subsequently, smoothing techniques, such as bi-harmonic transformation, are applied to convert discrete temperature measurements to continuous functions, so that the missing data measurements can be estimated. The bi-harmonic transformation has been widely used for the interpolation of three-dimensional (3D) discrete data with irregular boundary conditions (Sandwell, 1987; Gáspár, 1999; Hale, 2009). We further correlate the extracted melt pool characteristics to the locations of pores based on a Self-Organizing Map (SOM) clustering algorithm. We focus on abnormal melt pool behaviors satisfying either of the two key assumptions: (i) the thermal distribution of a melt pool causing porosity tends to exhibit different characteristics from other normal melt pools and (ii) the number of abnormal melt pools is small compared with normal melt pools. The output of the SOM groups the melt pool images into clusters based on the similarity of thermal distributions. Melt pools belonging to groups dissimilar to others tend to cause outliers of microstructure, such as mini-cracks and pores as shown in Figure 1. We validate our method by comparing the predicted locations of pores based on the melt pool temperature distribution and the actual locations of pores obtained via X-ray CT scanning. Results show high prediction accuracy and low false alarm rate.

One key issue is that the thermal images/history are related to porosity in the fabricated part in this study. For instance, if superheated or low-input-energy melt pools are observed during the build, corrective actions can be performed before the

next layer is built on. This identification reduces product cost, as the percentage of product waste will significantly decrease. Note that the choice of process variables is not explicitly considered to link with the thermal history/images. It can be argued that different set of process variables can also have a significant effect on thermal history. Nevertheless, it is beyond the scope of this study and will be investigated in future studies. However, a number of studies are available in the literature that investigate the control procedure for correcting defects and stabilizing the temperature distribution. Interested readers can read the work by Mireles *et al.* (2015) and Kruth *et al.* (2007) for more information.

The rest of this article is organized as follows. Section 2 provides a detailed literature review on the existing porosity detection techniques, as well as on the characterization of melt pool characteristics. Section 3 proposes the feature extraction methodology for modeling the thermal distribution of melt pools using functional data analysis tools. Section 4 gives a detailed discussion on the SOM methodology that is used to detect porosity. A case study of porosity detection of a Ti-6Al-4V thin wall based on the melt pool thermal characteristics is illustrated in Section 5. Finally, Section 6 discusses the conclusions from the present study.

2. Literature review

We survey the papers pertaining to melt pool monitoring and characterization as well as the existing porosity detection techniques. This section is divided into two subsections: (i) methods for porosity characterization and (ii) melt pool monitoring and modeling.

2.1. Literature on porosity characterization

2.1.1. Porosity prediction techniques based on post-manufacturing characterization

Ultrasonic and X-ray CT have been used extensively for porosity detection in materials such as stones (Tajeripour and Fekri-Ershad, 2012), ceramic materials (Eren *et al.*, 2012), and so forth. Ultrasonic methods have been primarily used for analyzing the porous structure and mechanical strength and to detect internal defects such as voids, cracks, delaminations, and many more (Lafhaj *et al.*, 2006; Goueygou *et al.*, 2009; Abraham *et al.*, 2012; Garnier *et al.*, 2013; Soltani *et al.*, 2013). Three different ultrasonic approaches have been applied by Eren *et al.* (2012) to characterize porosity, as well as for detection and imaging of different types of defects in ceramic materials. Air-coupled ultrasound can be implemented for non-contact detection and imaging of defects in ceramic tiles, despite the relatively high impedance of ceramic materials. Frequency dependence of attenuation can be used for the quantification of porosity, which is an important practical task in the ceramic industry. One interesting finding of that study was that measurements of ultrasonic wave velocity were found to be a reliable tool for the characterization of porosity in ceramic materials. Through experiments, the authors observed that a 5% porosity change in ceramic tiles results in a reduction of about 20% in ultrasonic wave velocity. However, the accuracy of ultrasonic characterization of porosity is sensitive to the selective layers of samples. It is thus not capable of capturing pores between two consecutive sample layers.

The majority of studies on porosity detection focus on post-manufacturing characterization using X-ray CT. Among the studies that discuss X-ray CT, Kowaluk and Woźniak (2012) investigated the measurement of pore volume in cast aluminum using a METROTOM 800 Carl Zeiss computed tomography system. The benefits of using flash thermography against other approaches such as ultrasonic attenuation estimation have been discussed by Meola and Toscano (2014), where the authors state that through flash thermography a part can be inspected while viewing either the smooth or the rough side. It is non-contact, cost-effective, and fast. Wells (2007) showed X-ray CT modality using advanced Volume Graphics StudioMax (VGSM) voxel analysis and visualization software for 3D defect characterization, analysis, and visualization. Defects of interest in this study were primarily porosity and some inclusions, resulting in a total defect level of 1.11% of the total casting volume. Cai *et al.* (2015) proposed an X-ray CT method that involves image enhancement and ring artifact removal before image segmentation. By using X-ray CT, the authors investigated the effect of process parameters on material porosity. Moreover, the obtained results were compared with the conventional Archimedes testing method and experimental results showed the superiority of X-ray CT.

The limitations of the post-manufacturing characterization approaches are that they are usually expensive and time-consuming. The accuracy of ultrasonic characterization depends on the layers selected for inspection. Moreover, post-manufacturing characterization of porosity does not leverage the unique layer-by-layer building mechanism of AM that allows for in-process correction/control of defects before the next layer is built.

2.1.2. Visual-based porosity detection techniques

Visual-based porosity detection refers to the detection of anomalies while building the part, which allows steps to be taken to correct them in real time. Tajeripour and Fekri-Ershad (2012) proposed an approach for porosity detection in stones by using an enhanced version of local binary pattern features. In this approach, a threshold is calculated from porosity-free images during a training phase. Using this threshold value, porosities are detected from the test images. Schwerdtfeger *et al.* (2012) investigated the possibility of *in situ* anomaly detection for a powder bed beam-based AM process. Ti-6Al-4V parts were built in a selective electron beam melting system, and during the fabrication of the parts, a number of infrared (IR) images were taken of different layers. Metallographic images of the same layers were also taken from the same material, resulting in its destruction. The authors observed a good correlation between the patterns visible in IR images and metallographic images. This correlation specifies that regions with higher heat radiation (lighter color in images) correspond to an anomaly in the part. Every anomaly visible in the IR images was also found in the metallographic images. This provides a unique procedure for *in situ* quality control for selective electron beam melting systems, as anomalies can be repaired in real time using appropriate repair methods such as re-melting of the compromised area or a combination of additional powder deposition and re-melting of the compromised area. Fan *et al.* (2010) proposed an

image processing methodology that uses optical system design to develop an online surface defect detection system. They also developed an analysis algorithm for an automatic defect classification technique. This algorithm removes noise from porous images, detects object edges, and uses a hybrid-based method to determine the defects (i.e., crevice, scratch, broken corner, and dent) in the parts. From the experiments conducted in that study, the authors found that the maximum miss rate can be controlled to be less than 5.65%. Clijsters *et al.* (2014) developed an *in situ* monitoring system for Selective Laser Melting (SLM) that consists of a photodiode and a near-IR thermal camera coupled with a data capture and processing system. This setup enables the user to log morphological data of the melt pool that are used to classify vectors into different zones of varying heat flow situations and/or parameter sets. The effectiveness of this method was validated using experimental data captured on manufactured Ti-6Al-4V, AlSi10Mg, and NiTiInol parts.

The limitation of visual-based methods used to detect porosity is that they are usually applied to detect pores with large sizes (e.g., diameter at the scale of hundreds of micrometers). The detection accuracy tends to be low for the detection of pores with small/medium sizes. Most of the visual-based detection approaches are based on images obtained from IR cameras, the accuracy of which is subject to emissivity and reflection issues. Extra efforts are required for the purpose of calibration.

2.2. Melt pool monitoring and modeling

A number of studies are available in the literature that discuss melt pool modeling in DED with varying degrees of detail. For instance, closed-form equations have been developed by Hunt (1984) to map material solidification boundaries by leveraging multiple solidification parameters and material composition. Although this classic approach was originally developed for metal casting, Kobryn and Semiatin (2001, 2003) subsequently showed that the maps are capable of predicting the microstructure obtained in Ti-6Al-4V via a laser AM process. Gockel *et al.* (2014) expanded on Hunt's curves to produce solidification morphology curves for Ti-6Al-4V in the process parameter space. Furthermore, Gockel *et al.* (2014) compared their results with a previously developed process map for the melt pool geometry that shows that maintaining a constant melt pool cross-sectional area yields a constant grain size. Additionally, the grain morphology boundaries were found to be similar to curves of constant melt pool aspect ratio. Khairallah *et al.* (2016) developed a mesoscopic model to investigate how the strong dynamical melt flow generates pore defects, material spattering (sparking), and denudation zones using the ALE3D multi-physics code. Surface tension, Marangoni effect, and recoil pressure are incorporated in the model. That study also explained in detail how three kinds of pore defects (depression collapse, lateral pores, open and trapped pores) are generated and strategies to avoid them are discussed. Shiomi *et al.* (1999) developed a finite element model to calculate the weight of a solidified part made of metallic powder. The authors reconstructed meshes after each heating cycle by several laser pulses and assumed the physical properties to be independent of temperature. Experimental and simulated results showed that the amount

of solidified parts after a pulse is affected by the peak power of the laser, rather than the duration of laser irradiation. Hu and Kovacevic (2003) developed a 3D heat transfer model using ANSYS and used it to study the thermal behavior of the melt pool in building a single-bead stainless steel wall via a closed loop-controlled laser-based powder deposition process. The model provides the magnitude of laser power required to maintain a constant width of the melt pool.

The width and depth of the melt pool are expected to affect porosity caused by lack of fusion. The area of the melt pool may also affect the concentration of porosity caused by oxides. The melt pool depth is also crucial to the thickness of deposited layers, the microstructure evolution, and pore formation. High layer thickness values tend to result in lack of fusion between successive layers and adjacent tracks. This has been studied by Cunningham *et al.* (2017), Dilip *et al.* (2017), Tang *et al.* (2017), and many more. More specifically, Cunningham *et al.* (2017) and Dilip *et al.* (2017) demonstrated that the width and depth of the melt pool have a significant impact on the formation of porosity in the fabricated part. Cunningham *et al.* (2017) showed that the ratio of hatch spacing to the width of the melt pool can be important. Too small a ratio can induce keyhole porosity, even if power and velocity values are not sufficient to induce keyhole porosity by themselves. However, too large a ratio can yield a lack of fusion porosity, due to fluctuations in melt pool dimensions, even in cases where the overlap depth would otherwise be sufficient. On the other hand, Dilip *et al.* (2017) focused on the evolution of single-track melt pools and porosity in parts made of Ti-6Al-4V alloy using SLM. The single-track deposits were made using variable laser power and scan speeds, and their effects on the melt pool morphology were studied. Microstructural studies on the melt pool cross-section showed that at a low power level and high scan speed, the width of the track reduces, gradually becoming discontinuous and eventually resulting in balling. The depth of penetration of the melt pool was observed to increase with a lower scan speed. At higher power levels, in some cases a keyhole effect is observed. Figure 1 shows the formation of pores due to different melt pool characteristics. Note that the quantitative thermal-porosity relationship is essential to identifying operation conditions and in-process control/diagnosis of AM processes for better part quality (Soylemez *et al.*, 2010; Gockel *et al.*, 2014; Thompson *et al.*, 2015).

Furthermore, Boddu *et al.* (2001) presented a review of the control of laser cladding for rapid prototyping. The authors demonstrated that dimensional analysis can be used as a modeling tool for predicting deposited layer thickness in direct metal deposition technique. An apparatus with a laser light source was used by Vetter *et al.* (1994) in a study of the laser cladding parameters. This study identified the position of phase changes in the powder but did not explicitly measure powder concentrations, inferring the position of the maximum concentration from power transmission along the axis. Nassar *et al.* (2014) and Siddique *et al.* (2015) have both presented defect location and pore size data measured using X-ray CT with optical cross-sectional metallography. Nassar *et al.* (2014) compared their data to another method of *in situ* defect detection using optical emission spectroscopy. Siddique *et al.* (2015) critiqued the two

methods demonstrated by Nassar *et al.* (2014); in particular, they noted that due to the lack of any significant differences between the techniques, the X-ray CT data must be favored, due to the non-destructive nature of CT. However, a discrepancy between data sets can be observed if X-ray CT data are chosen, and the acquisition process is substantially more expensive compared with cross-sectional optical microscopy. Ding *et al.* (2016) provided a solution to the challenges of process reliability and the repeatability of finished components by developing a sensing and control system for the robotically controlled eight-axis laser-based direct metal addition system. Moreover, an IR imaging setup was installed on the laser head to monitor the top full-field view of the melt pool. To build a closed-loop control system to achieve a uniform melt pool size, a simple proportional–integral–derivative controller coupled with feed-forward compensation was used. A thermo-mechanical model of directed energy deposition AM for Ti-6Al-4V was developed by Heigel *et al.* (2015) that utilizes measurements of the surface convection generated by gases flowing during the deposition. More specifically, this work highlights the importance of having a detailed knowledge of the surface heat transfer to produce more accurate finite element analysis results. Moreover, an additional model was proposed that uses the assumption of free convection on all surfaces. Numerical results showed that a measurement-based convection model is required to generate error-free simulation results.

2.2.1. Melt pool characterization based on morphological characteristics

Among the methods that focus on melt pool morphological features (e.g., size, length, area, etc.), Birnbaum *et al.* (2003) investigated issues related to control of melt pool size in Laser-Based AM (LBAM) based on a process map approach that relates process parameters to the melt pool size. Also, Qi *et al.* (2006) investigated various morphological features of melt pools and studied physical phenomena related to it. They proposed a model for the motion of the melt pool's free surface in uninterrupted cladding and benchmarked their findings against practical results based on the melt pools' width, length, and height of the solidified cladding track. Similar approaches can be found in Kim and Peng (2000) and Pinkerton and Lin (2004). Ahn *et al.* (2017) proposed a novel method for evaluating the characteristic length of the melt pool. The efficacy of two evaluation methods was analyzed and the method using the gap between the two centers of neighboring scans was experimentally found to be more efficient, due to the averaging effect. Wang *et al.* (2017) took a unique approach where they developed a physics-based multivariable model for directed energy deposition. Using the conceptual framework provided by Dumanidis and Kwak (2001), these authors parameterized the material transfer rate in the deposition as a function of the process operating parameters. This in turn improved the characterization of the interdependence between the melt pool height and laser power. Clijsters *et al.* (2014) developed an *in situ* monitoring system for SLM that leverages morphological features such as melt pool area, length, width, and intensity. Li *et al.* (2017) provided a comparative study of the

LBAM of Inconel 718 using the pulsed-wave and continuous-wave laser modes by both simulations and experiments. A 3D numerical model was developed and investigated in simulations of the transient melt pool motion, heat transfer, and fluid flow for pulsed-wave LBAM. There are two essential findings of the study: (i) simulated single-track melt pool geometries and average temperatures under both laser modes are in good agreement with measured results in the study and (ii) the solidification front in the pulsed-wave case is about 15° more tilted to the laser scanning direction compared with the continuous-wave case.

2.2.2. Melt pool monitoring based on thermal characteristics

Another stream of research utilizes thermal characteristics for the purpose of monitoring and closed-loop control (Tang and Landers, 2010). Chandrasekhar *et al.* (2015) applied IR-thermal images of a weld pool to find a smart method to model the weld beams' penetration. More specifically, the authors developed hybrid intelligent models, combining image processing with soft computing techniques, such as an adaptive neuro fuzzy inference system and artificial neural network, to estimate the width of the weld bead and the depth of penetration using the thermal image of the weld pool. Bi *et al.* (2006) have investigated the deposition of thin walls with constant laser power and different process control strategies. They primarily focused on the emitted signals of melt pools from IR-temperature and found that both the size and temperature of the melt pool influence the dimensional accuracy of the deposited sample. The authors concluded that these signals can be used for closed-loop and part quality control as well as for process monitoring. Hua *et al.* (2008) have investigated the effects of laser processing parameters on the temperature of melt pools. The investigation resulted in a relationship between melt pools and the thickness of the cladding layer. A relationship between the melt pool and the thickness of the cladding layer that results in a scheme to achieve accurate *in situ* control for the layer thickness was also discussed. This was achieved by using an analytical model based on temperature measurement of the melt pool. Song *et al.* (2012) applied a hybrid control system to reinforce the quality and precision of geometrically complex parts in accordance with the temperature of the melt pool. The cladding height controller developed in that study was a rule-based controller, whereas the melt pool temperature controller was a generalized predictive controller with input constraints. These two controllers were connected in series, with the height controller given a higher priority compared with the temperature controller. Picasso and Hoadley (1994) presented a Finite Element Method to analyze the effects of powder injection and thermocapillary on melt pool shape and fluid movement.

The limitation of the existing melt pool models is that they are primarily developed based on deterministic physics-based differential equations. These equations do not capture the variations and uncertainty associated with the underlying thermo-physical process during the build and thus tend to deviate from reality. The existing melt pool monitoring/modeling approaches focus on simple metrics, such as the size, length, peak temperature, etc. There is a lack of comprehensive characterization for

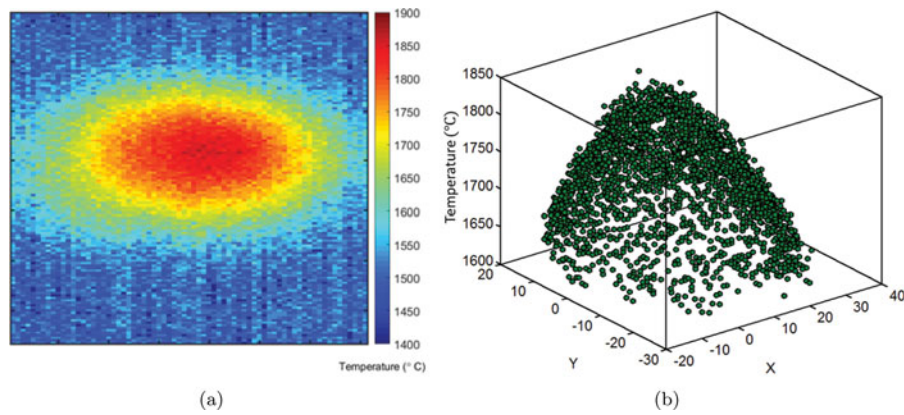


Figure 2. Modeling the characteristics of a melt pool during the build: (a) the contour plot of the melt pool in pixels and (b) thermal distribution of the top surface of the melt pool.

the distribution of temperature over the top surface of the melt pool. As a result, the extracted features may be limited. Porosity prediction based on such simple metrics may not be accurate.

In summary, the technical contributions of this study to the existing literature are as follows:

1. We develop a novel methodology to investigate the thermal–porosity relationship from a data mining perspective. This work is significant since the existing approaches for porosity detection mainly rely on post-manufacturing approaches, which can be expensive and time-consuming. More important, post-manufacturing characterization does not allow for the detection and correction of porosity during the build, resulting in lower product quality.
2. We develop a novel data processing procedure that converts each thermal image into a function, which can be processed using advanced statistical analysis tools. Compared with the existing literature that mainly utilizes simple metrics of the melt pool, our proposed study provides a new tool for leveraging the comprehensive thermal distribution.
3. The proposed methodology is among a handful of studies available in the literature that provides a theoretical foundation for qualification and certification of AM products via the temperature distribution of the melt pool.

3. Modeling of thermal images of the melt pool

3.1. Characteristics of the image data of the melt pool

We focus on modeling the thermal image data streams obtained during the fabrication of parts using a Laser Engineering Net Shaping (LENS) system. LENS is a means to build metallic prototypes/parts by combining the material and energy delivery for simultaneous deposition and part forming. LENS does not rely on a pre-deposited layer of metallic powder and thus may be used as a means to repair or coat parts via cladding. In addition, due to the combined material/energy delivery method, LENS can be readily utilized to create functional graded/composed parts with varying material/alloy concentrations. Finally, pre-form mixing such as coaxial powder delivery can be accomplished with LENS (Thompson *et al.*, 2015).

Melt pool images are captured, in real time, using a high-resolution Stratonics ThermoViz multi-sensor system, including a two-wavelength imaging pyrometer for melt pool monitoring and an IR thermal imaging sensor for global heat flow monitoring. The data are recorded in an image format where each pixel corresponds to a discrete measurement of the melt pool temperature. An example of the melt pool image is shown in Figure 2(a). Figure 2(b) shows the scatter plot of temperature measurements.

Processing and modeling the thermal image data is very complex. Major challenges include (i) the thermal imaging system generates a tremendous amount of data. A small single-track thin wall may result in over 10 GB of thermal image data; (ii) the signal-to-noise level is so low that the boundary of the melt pool is not clear in the thermal images, as shown in Figure 2(a); (iii) the size and center of melt pools vary during the build; hence, extra efforts are needed to align the melt pools and account for various melt pool sizes; and, finally, (iv) temperature measurements may be missed during data acquisition.

3.2. Modeling the thermal distribution of melt pools

We propose a modeling procedure that converts melt thermal images to continuous temperature models with the identical function support. Image processing is applied to extract the temperature distribution of the top surface of each melt pool from the captured melt pool images. Extracted data points are converted into spherical coordinates. Subsequently, a non-parametric surface interpolation method is implemented on the extracted temperature distribution of the top surface of each melt pool. The resulting continuous temperature, modeled with identical function supports, will be used as input for melt pool clustering in Section 4. The details of the melt pool modeling are as follows.

1. *Data rescaling:* Data captured by the system contain a columns and b rows, which are determined by the resolution of the captured image. We denote the row and column by X and Y , respectively, where (X, Y) represents coordinates in the melt pool image that correspond to temperature measurement $T(X, Y)$. The melting temperature is denoted by T_γ , which is pre-specified based on material properties. The points (X, Y) with temperatures greater than T_γ are extracted. The resulting

temperature measurements define the region of the melt pool surface; i.e., $M = \{(X, Y) : T(X, Y) \geq T_\gamma\}$.

Next, we rescale the data within the melt pool based on the melting temperature T_γ and peak temperature, denoted by T_{max} . Assume that the coordinates of the peak temperature are denoted by (X_p, Y_p) . We define the range of temperature by $R = T_{max} - T_\gamma$ for the melt pool. We centralize the melt pool shape in peak temperature and also scale temperature between zero and one (Equation (1)):

$$(X^c, Y^c, T^s) = \left(X - X_p, Y - Y_p, \frac{T - T_\gamma}{R} \right) \text{ for } (X, Y) \in M. \quad (1)$$

Here, c represents the centralized melt pool in peak temperature and s accounts for the scaled temperature to the interval between zero and one.

2. **Spherical transformation:** To apply to the tool of functional data analysis, we convert the triplet of (X^c, Y^c, T^s) to the spherical domain (θ, φ, ρ) , where θ and φ represent the angles within the X - Y plane and the T - XY plane, respectively. ρ represents the radius. The mathematical expressions of the spherical transformation, denoted by s , is shown below:

$$(\theta, \varphi, \rho) = s(X^c, Y^c, T^s) = \left(\arctan\left(\frac{Y^c}{X^c}\right), \arccos\left(\frac{T^s}{\sqrt{(X^c)^2 + (Y^c)^2 + (T^s)^2}}\right), \sqrt{(X^c)^2 + (Y^c)^2 + (T^s)^2} \right).$$

The visualization of the temperature distribution of the top surface of the melt pool boundary with spherical coordinates is shown in Figure 3(a). Once the spherical transformation is applied, all of the temperature measurements are converted to function values defined in the region of $(\theta, \varphi) \in [-\pi, \pi] \times [0, \pi/2]$.

3. **Interpolation via bi-harmonic surface interpolation method:** The bi-harmonic surface fitting method is applied for data interpolation and smoothing; it converts the discrete data points to a continuous function as shown in Figure 3(b). Subsequently, an equally

spaced grid (e.g., 50×50) on (θ, φ) is defined to obtain discretized measurements of the melt pool temperature.

The proposed data processing procedure transforms melt pool thermal images, containing missing values and ill-structured data, to standardized vectors of temperature measurements of the same length and are defined on the identical function support, denoted by \mathbf{m}_i for $i = 1, \dots, N$. In the next section, the SOM clustering algorithm is applied to \mathbf{m}_i s to identify the anomalies of melt pools by capturing the similarity and dissimilarity.

4. Porosity prediction using SOM clustering

We apply an SOM model with size $z \times z$ to the set of standardized melt pool vectors $\mathbf{M} = \{\mathbf{m}_i : i = 1, \dots, N\}$ obtained in the previous section. SOM is a type of unsupervised machine learning neural network that uses a procedure called competitive learning to discern patterns (Jafari-Marandi and Keramati, 2014). The SOM maps high-dimensional input data into a two-dimensional (2D) space, while preserving the topological interrelationship between data. Note that the mapping does not change the relative distance or similarity among data points (Pratiwi, 2012; Patel and Giri, 2016). The clustered data reduce the dimensionality and intuitively characterize the similarity among data points. In essence, the method works best for unsupervised learning tasks and its superiority lies in its visual presentation of the data. Since we have multidimensional data, dimensions of which need to be reduced as well as similarity among them needing to be captured and characterized, SOM is the perfect fit for this study. Note that SOM has been used as a linking step between image data pre-processing and porosity prediction. Moreover, in this study, leveraging the SOM maps, a correlation matrix is created based on the centroid vector that identifies the level of correlation of each cluster to all the others. Afterwards, the correlation and the number of melt pools in each cluster determine whether the cluster consists of normal or abnormal melt pools.

The SOM clustering outputs z^2 clusters with the center of each cluster as well as melt pools belonging to each cluster. The algorithm provides a brief overview of the SOM algorithm. More detailed discussion can be found in Merényi *et al.* (2016), Patel and Giri (2016), and Chowdhury *et al.* (2017).

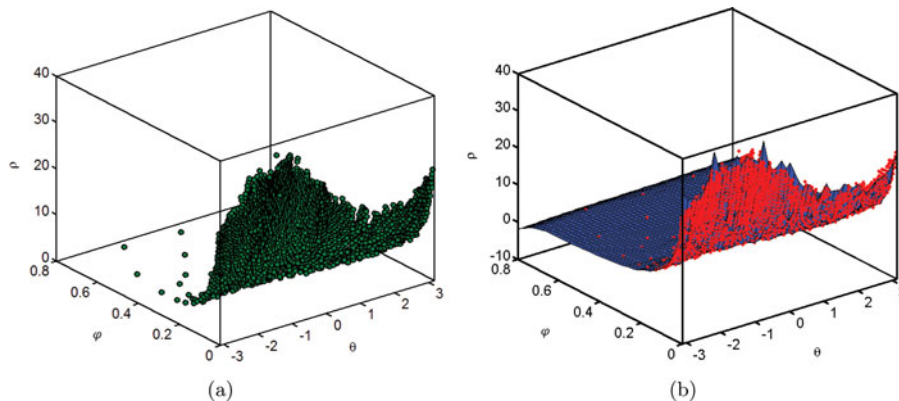


Figure 3. Plots of (a) the temperature distribution at the top surface of the melt pool and (b) the interpolated temperature distribution of the melt pool using the bi-harmonic surface interpolation method. Both plots are in spherical coordinates.

Algorithm. Melt pool clustering via SOM

Input data. Set of interpolated features $\mathbf{M} = \{\mathbf{m}_i : i = 1, \dots, N\}$.

Steps.

Initialization. At iteration $e = 0$, randomly generate a weight coefficient vector for each cluster using a uniform distribution. The resulting weight coefficient vectors, at iteration $e = 0$ are denoted by $\mathbf{w}_j(0)$ for $j = 1, \dots, z^2$. We also specify a decreasing, non-negative learning rate function $\alpha(e)$, which controls the convergence of the SOM algorithm.

Model training. For each iteration e , update weight coefficient vectors $\mathbf{w}_j(e)$ s according to Steps 1 to 5 below.

1. Randomly sample a melt pool thermal vector \mathbf{m}_i from the thermal data set \mathbf{M} without replacement.
2. Calculate the Euclidean distance between \mathbf{m}_i and all weight coefficient vectors $\mathbf{w}_j(e)$ as shown below:

$$\delta_j = \|\mathbf{m}_i - \mathbf{w}_j(e)\| \quad j = 1, 2, \dots, z^2.$$

3. Choose the best matching cluster by minimizing distance δ_j . That is, $\delta_{j^*} = \min_{j=1, \dots, z^2} \delta_j$, where j^* is the index of the best matching cluster. The melt pool image represented by \mathbf{m}_i is assigned to the best matching cluster j^* .
4. Update the weight coefficients in the neighborhood of cluster j^* , denoted by $V(j^*)$, according to the formula below:

$$\mathbf{w}_j(e) \leftarrow \mathbf{w}_j(e) + \alpha(e)[\mathbf{m}_i - \mathbf{w}_j(e)] \quad j \in V(j^*).$$

5. If all of the melt pool vectors in \mathbf{M} have been sampled, set $e \leftarrow e + 1$. Otherwise, go to Step 1.

Stop when the vectors of the weight coefficients converge. That is, $\mathbf{w}_j(e) \rightarrow \mathbf{w}_j$, for $j = 1, \dots, z^2$. Specifically, the process is stopped if the absolute difference between the weight vector at iterations $e + 1$ and e is small, typically less than 1% (Fritzke, 1995).

The output of the SOM is a $z \times z$ 2D map that illustrates the number of melt pools in each cluster and the distance among adjacent clusters. Figure 4(a) provides an example of an SOM hit map demonstrating the population size of each cluster. Figure 4(b) indicates neighbor weight distances among these

clusters. The darker color in Figure 4(b) means cluster dissimilarity, whereas the lighter color means the opposite. We can also estimate the correlation between all the pairs of clusters:

$$\text{Corr} = \begin{bmatrix} d_{1,1} & \dots & d_{1,z^2} \\ \vdots & \ddots & \vdots \\ d_{z^2,1} & \dots & d_{z^2,z^2} \end{bmatrix},$$

where $d_{r,w} = \text{Corr}(\mathbf{w}_i, \mathbf{w}_j)$ for $i, j = 1, 2, \dots, z^2$.

An abnormal cluster satisfies two conditions: (i) it is not highly correlated with other clusters and (ii) the number of melt pools belonging to this cluster is low. We use the median value to characterize the correlation of a cluster to the others (the median of each row of the correlation matrix). We identify a cluster as an anomaly when its median correlation and the percentage of melt pools are low.

5. Case study

In this section, we aim to validate the accuracy of the proposed porosity prediction methodology based on melt pool anomalies. A single-track Ti-6Al-4V thin wall is built using an OPTOMECH LENS 750 system with the thermal history recorded. The predicted distribution of porosity of the as-built part, based on melt pool characteristics, is compared to the results of X-ray CT characterization. We examine the accuracy of the porosity prediction by investigating the percentage of pores successfully predicted based on melt pool clustering, as well as the false alarm rate, by looking into the percentage of normal melt pools that are predicted to cause porosity. We compare the performance of this method with a previous work that focuses on only the morphological features of melt pools (Khanzadeh *et al.*, 2016). A discussion about the model selection of SOM is also provided to determine the size of SOM models.

5.1. Experimental set-up

An OPTOMECH LENS 750 machine equipped with a 1-kW Nd:YAG laser, pyrometer, and in-chamber thermal camera (Fig. 5(a)) is used to fabricate single-track Ti-6Al-4V thin walls (Fig. 5(b)). LENS has become a popular means to accomplish powder-based Direct Laser Deposition due to its capability to

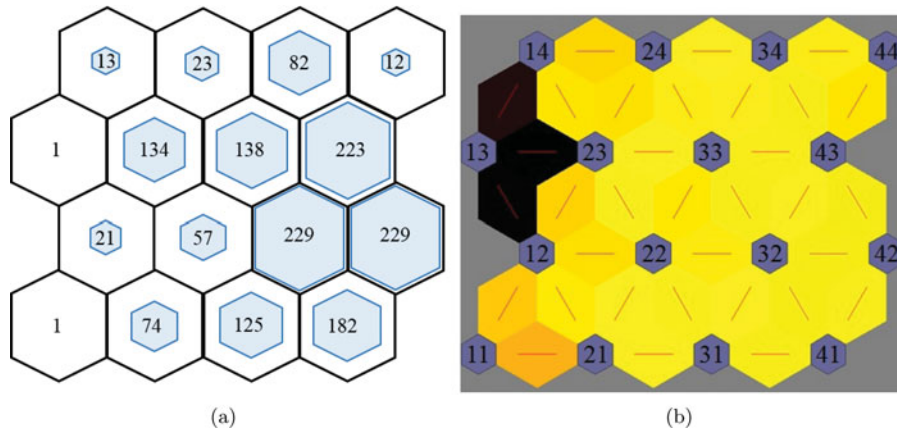


Figure 4. SOM for the proposed melt pool model, which includes (a) mapping each melt pool profile into a different cluster and (b) weighting the distances between neighboring clusters.

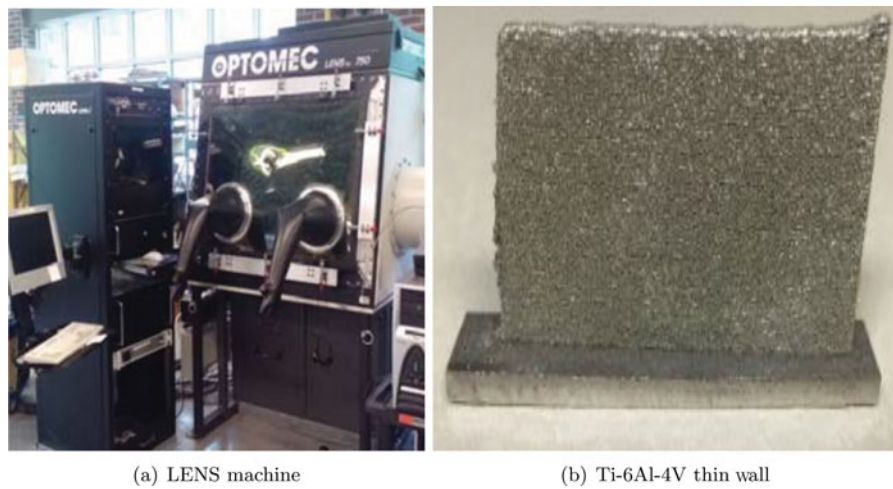


Figure 5. Fabricated Ti-6Al-4V thin wall using LENS machine.

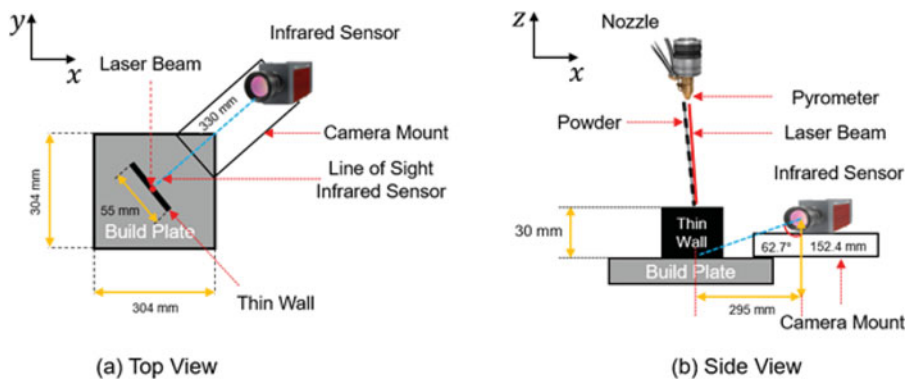


Figure 6. Images of (a) the top view of the IR camera and (b) the side view of the pyrometer and their orientation with respect to the substrate and the thin wall within the build chamber (Marshall *et al.*, 2016).

create functionally graded materials (Shamsaei *et al.*, 2015; Thompson *et al.*, 2015). Processing conditions of the LENS machine used to manufacture the Ti-6Al-4V thin wall are provided in Table 1.

The time-varying evolution of melt pool behaviors is captured by the built-in thermal imaging system and is then used to predict the porosity distribution based on melt pool clustering. A dual-wavelength pyrometer (Stratronics, Inc.) and an IR camera (Sierra-Olympic Technologies, Inc., Viento320) are used to capture the temperature distribution of the top surface and the side view of the melt pool during manufacture (see Fig. 6). Since we are using the information from the top surface of the melt pool in this study, data obtained solely from the dual-wavelength pyrometer are used for porosity prediction. The advantage of using the pyrometer sensor is that it reduces the risk of motion blur, as the pyrometer has a specified exposure time (2.0274 ms) that occurs at a specified collection rate. The scan rate of the laser is 12.7 mm/s. Moreover, during the exposure time, the build moves at approximately 26 μm (Marshall *et al.*, 2016). The IR camera is typically used to capture the characteristics of

the melt pool from the side view. Hence, collecting melt pool data from the IR camera and its calibration is not needed in this study. The pyrometer is mounted above the OPTOMECH LENS 750 machine, outside of the inert environment of the chamber, and is aligned to view down the laser shaft via a series of three broadband metallic mirrors. A CMOS detector is used in the pyrometer with an array size and pixel pitch of 752×480 and 6.45 μm , respectively. The temperature range in the pyrometer varies from 1000 to 2500°C. Exposure time and pixel clock are set to be 2.0274 ms and 5 MHz, respectively. The nominal image collection rate of the pyrometer is approximately 6.4 Hz (see Fig. 6(b)). The IR camera is oriented at approximately 45° with respect to the sides of the CNC stage and is tilted in such a way that the focal plane is rotated 10° from a line normal to the substrate. The thin wall is constructed at an orientation such that one of its sides is fully in view of the IR camera. The nominal image collection rate of the IR camera is approximately 12.58 Hz. This allows the melt pool images to be captured in real time. Each melt pool image has a 1.7 MB file size. Hence, with such high image resolution and monitoring frequency, a single thin-wall build

Table 1. LENS processing parameters for AM thin wall.

Power	300 W	Substrate (stainless steel)	3.175 mm
Scan speed	30 rpm	Starting offset from substrate	130.391 mm
Powder feed rate	0.9 rpm	Determination of layer thickness	0.508 mm
Determination of hatch spacing	0.508 mm	Nozzle diameter	0.889 mm

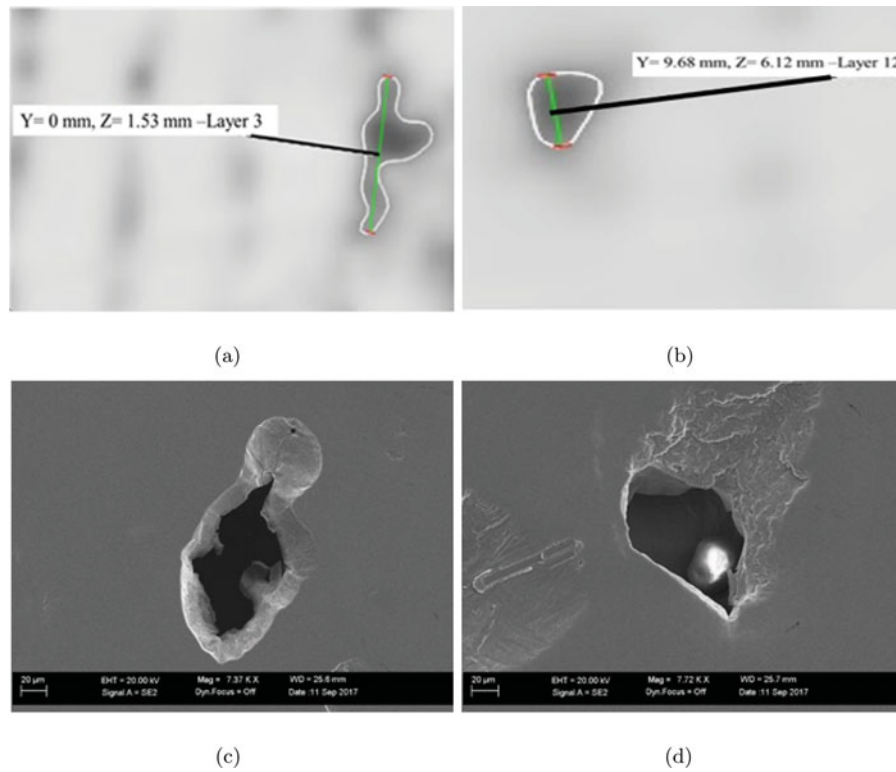


Figure 7. Illustrating instances of X-ray CT scan (a and b) and SEM micrograph (c and d).

(length = 47.81 mm, height = 27.56 mm, thickness = 1.78 mm) results in 4.7 GB of image stream data (Marshall *et al.*, 2016).

The microstructure is also characterized using X-ray CT, which captures numerous X-ray images around an axis of rotation and reconstructs a digital 3D model of the part. The CT method used in this study utilizes a full 3D cone of X-rays with a 2D detector. This cone beam scanner irradiates the part as it moves in a 360° circle around the part, acquiring data throughout the scan. After the data are collected, a radon transform is applied to reconstruct the image using the acquired X-ray intensity readings for each of the detector elements. The individual slice images can then be accumulated into a 3D reconstruction (Hsieh, 2003). Despite the long processing time, X-ray CT is capable of accurately identifying the sizes and locations of pores (Kruth *et al.*, 2011; De Chiffre *et al.*, 2014). Therefore, we use the outcomes of X-ray CT characterization as the benchmark of our prediction method. Moreover, a scanning electron microscope (SEM; FEG SEM Zeiss SUPRA 40) is used to detect pore surfaces of the thin wall, which is Au/Pd sputter-coated, to determine the crack initiation sites and crack propagation characteristics. Instances of an X-ray CT scan and SEM micrograph are provided in Figure 7.

5.2. Porosity prediction using melt pool temperature distribution characteristics

The thermal image data are processed and stored in $N = 1564$ thermal image files, each of which contains 480×752 cells of information. In other words, $N = 1564$ represents the number of captured melt pools in the thermal history of the thin wall. The area of the melt pool is extracted based on the melt pool temperature of Ti-6Al-4V ($T_\gamma = 1636^\circ\text{C}$). Each melt pool is

centralized and scaled using the coordinates of the peak temperature. Based on the data processing procedure described in the previous section, each melt pool image is converted to a continuous thermal distribution model defined in the spherical domain of $(\theta, \varphi) \in [-\pi, \pi] \times [0, \pi/2]$. SOM clustering is then applied to the resulting thermal distribution models to obtain the clusters of melt pools.

Recall that we assume that (i) an abnormal melt pool has low correlation with others and (ii) the percentage of abnormal melt pools is much smaller compared with normal melt pools. Normal clusters should include a large number of melt pools that are similar to each other. We first examine the correlation between any two clusters represented by a correlation matrix. An example of the correlation matrix of a 4×4 SOM map is shown in Figure 8, which is a 16×16 symmetric matrix. The horizontal and vertical axes represent the labels of the clusters. The red color represents higher correlations, whereas the blue color corresponds to lower correlations. A cluster with low correlation to all others is considered to be an anomaly and porosity tends to occur at the corresponding locations. Cluster C21 demonstrates an example of a normal melt pool cluster, which includes a large number of melt pools highly correlated with other clusters. On the other hand, clusters C13 and C44 have low correlations with the other clusters. A melt pool in cluster C13 shows a higher temperature and irregular shape. Similar overheating is observed in the melt pool images belonging to cluster C44.

We calculate the median correlation of each cluster with other clusters and percentage of melt pools belonging to each cluster. The results are summarized in Table 2. Clusters C13, C14, C24, and C44 have the lowest median values, as well as the lowest percentage of melt pools. Also, the percentage of melt pools belonging to each of these clusters is below 1.5% of all melt pools. We also note that, although the median correlation

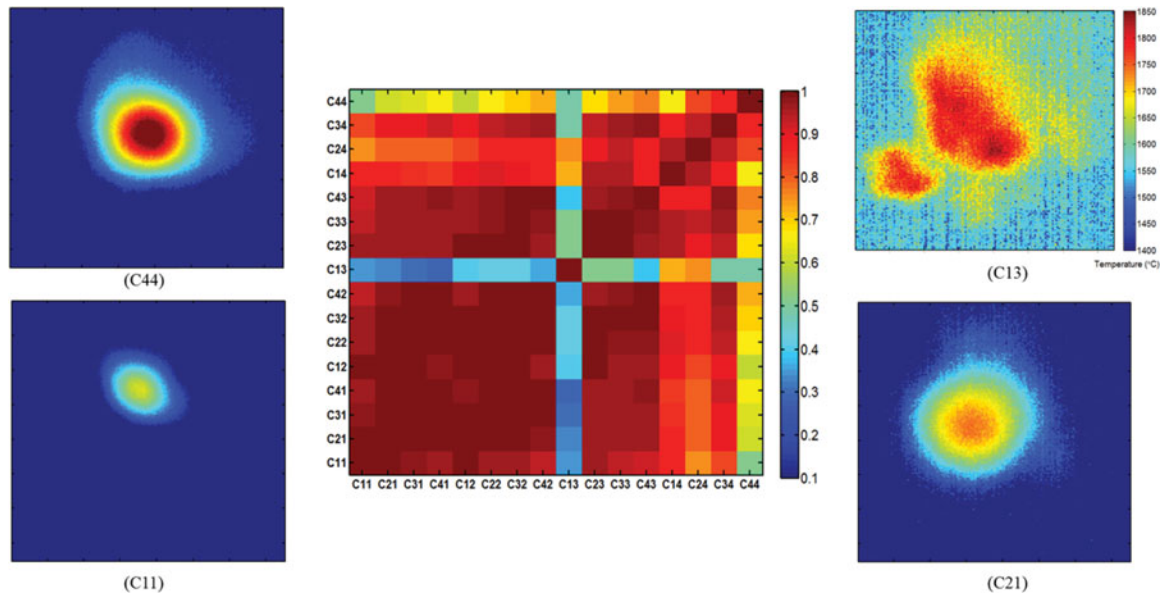


Figure 8. Correlation matrix (Cor) showing how pores were identified in the present methodology for the 16 clusters (Corr) of the 4×4 SOM map. Thermal profile images are shown with (C13, C44, and C11), which are the porosity clusters (poor correlation with other melt pool profiles) and the (C21) is a regular melt pool (more normal melt pool profile).

Table 2. Cluster correlation and percentage of melt pool in each cluster in 4×4 SOM model.

Melt pool cluster	C13	C44	C24	C14	C34	C11	C33	C23	C43	C41	C31	C42	C21	C12	C22	C32
Median correlation	0.41	0.67	0.86	0.88	0.93	0.95	0.97	0.97	0.97	0.97	0.98	0.98	0.98	0.98	0.99	0.99
Percentage of melt pool	0.06	0.77	1.48	0.84	5.28	0.06	8.88	8.62	14.35	11.71	8.04	14.74	4.76	1.35	3.67	14.74

Note: Bold numbers account for the clusters are chosen by decision rules and hypothesis.

between cluster C11 and others is not low, this cluster includes only one melt pool with a percentage of 0.06%. This cluster is also considered an anomaly, as there is no other melt pool sharing similar characteristics. Low energy input is observed from melt pool images from cluster C11, which tends to result in lack of fusion. As a result, these five clusters are considered to be anomalies. The other clusters have relatively high correlation (above 0.9) and include a larger number of melt pools and are thus considered normal.

The locations of predicted abnormal melt pools are compared to X-ray CT characterization, as shown in Figure 9. Each dot represents a pore characterized via X-ray CT and each square represents a pore predicted via the proposed melt pool-based method. The size of the dot/square indicates the actual size of the pore, the diameter of which ranges from 0.05 to 0.93 mm. The X-ray CT characterization identifies a total of 51 pores in the thin wall build, 47 of which are successfully predicted based on our proposed melt pool clustering method using a 4×4 SOM, resulting in a 92.16% prediction accuracy. Our prediction only results in three false alarms out of 1554 melt pools, resulting in a false alarm rate of 0.193%. In other words, only three melt pools out of 1554 are identified as anomalies without resulting in pores at the corresponding location. The false alarm may be partially attributed to the small sizes of potential pores that cannot be detected by X-ray CT.

We fabricate nine more samples to validate the efficiency of our proposed method as well as to show its generality. We employ the same methodology to those nine thin walls, but here we only show an example of those parts. Results show that when the same methodology is applied with 4×4 model, it

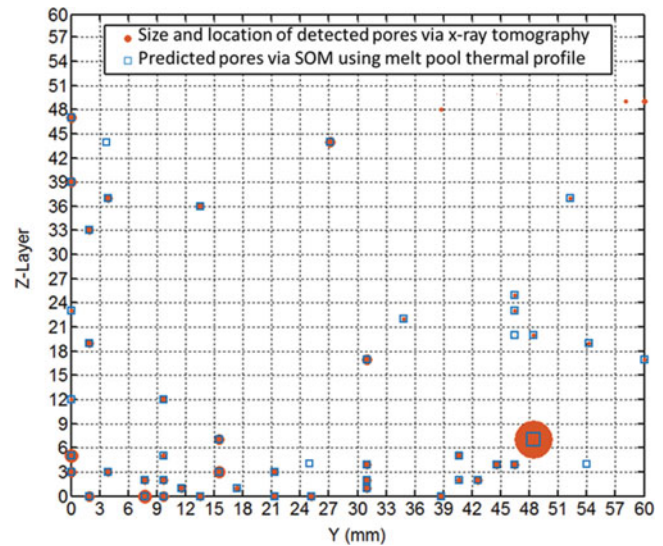


Figure 9. Plot of the various pores as a function of position within the AM thin wall. The predicted pores using the melt pool temperature distribution are shown against pores detected with X-ray CT. The size of the circle/square represent the size of pores.

demonstrates the same behavior as before in detecting anomalies (see Fig. 10 and Table 3). The highest percentage of abnormal melt pools in a single cluster is 1.33% for the 4×4 SOM model, whereas the median of correlation is less than 0.9. This is similar to the results obtained in Table 2. However, the results of the SOM models for this thin wall could not be validated via X-ray CT as it is expensive, time-consuming, and oftentimes not readily available. However, the pattern of SOM maps obtained through the proposed methodology for the new thin wall follows

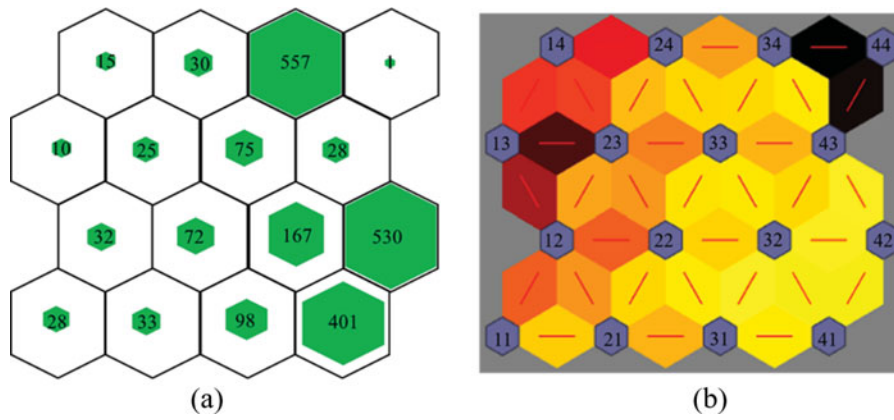


Figure 10. SOM of melt pool thermal profile for 4×4 model with new thin wall.

Table 3. Cluster correlation and percentage of melt pool in each cluster in 4×4 SOM model with new thin wall.

Melt pool cluster	C44	C43	C13	C11	C14	C12	C33	C24	C42	C43	C31	C34	C41	C21	C32	C22
Median correlation	0.35	0.88	0.88	0.92	0.93	0.93	0.93	0.94	0.94	0.94	0.95	0.96	0.96	0.96	0.97	0.97
Percentage of melt pool	0.05	0.48	1.33	1.33	0.71	1.52	3.57	1.43	25.21	1.19	4.66	26.50	19.08	1.57	7.94	3.43

Note: Bold numbers account for the clusters are chosen by decision rules and hypothesis.

the same trend as observed for the original thin wall in this study (see beginning part of Section 5.2). Hence, it can be stated that the developed methodology is suitable for different thin walls.

5.3. Model selection of SOM

We investigate various sizes of the SOM models in terms of prediction accuracy and false alarm rate for 4×4 , 5×5 , 6×6 , and 7×7 SOM models. The results are summarized in Table 4. With the same anomaly detection criteria, these four models result in 92.16, 92.16, 96.07, and 80.39% prediction accuracy, coupled with 0.193, 0.000, 0.128, and 0.000% false alarm rates, respectively. The 6×6 model results in the highest prediction accuracy of 96.07%. The prediction accuracy decreases when the model size increases. The false alarm rate is generally low (less than 0.2% for all four models). As a result, we recommend using a 5×5 or 6×6 model, which will further improve the performance of the porosity prediction as presented in Figure 9. SOM results for the 5×5 , 6×6 , and 7×7 models can be found in the Appendix (Figs. A1–A6). The correlation between clusters and percentage of melt pools belonging to each cluster can also be found in the Appendix (Tables A1–A3).

5.4. Comparison with melt pool monitoring based on morphological features

We compare our method with a previous study (Khanzadeh *et al.*, 2016) that focuses on the morphological features of the melt pool, such as the length, size, width, etc. Such features have been commonly used to monitor the stability of the melt pool and melt pool signal anomalies and perform closed-loop control (Doumanidis and Kwak, 2001; Qi *et al.*, 2006; Ahn *et al.*, 2017; Wang *et al.*, 2017). In a previous study (Khanzadeh *et al.*, 2016), we extracted the boundary of each melt pool, which contains information relevant to the length, width, area, and other simple morphological features. A similar SOM clustering algorithm is applied to identify anomalies based on the

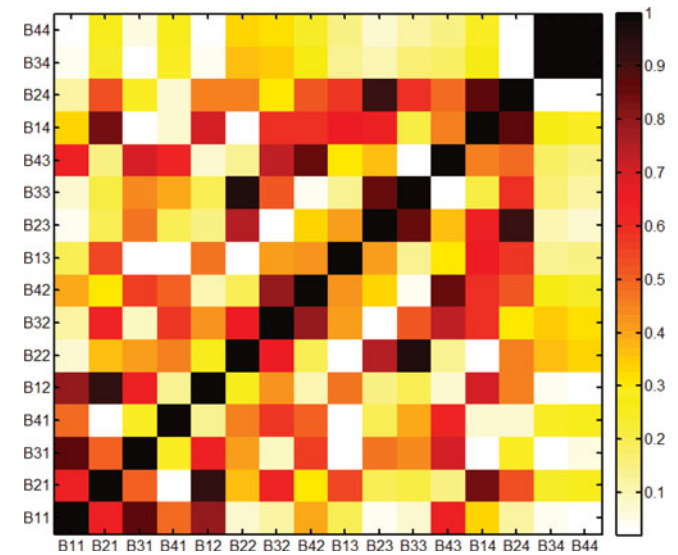


Figure 11. Correlation matrix (Cor) showing how pores were identified with morphological model of the top surface of the melt pool for the 16 clusters (Corr) of the 4×4 SOM map.

morphological features. The correlation matrix of a 4×4 SOM is shown in Figure 11. Unlike Figure 8, this correlation matrix does not show clear partitions of the clusters other than B34 and B44. It is clear that clusters B34 and B44 have very low correlations with the others. However, the remaining clusters do not clearly suggest anomalies.

Porosity prediction based on the morphological features of the melt pool is also performed using 5×5 , 6×6 , and 7×7 SOM models. The results are summarized in Table 5. The comprehensive study of four different SOM models shows that, using the same anomaly prediction criteria, porosity prediction based on morphological features results in less than an 83% prediction accuracy. The false alarm rate also significantly increases compared with the scenario where the thermal distribution within the melt pool is fully utilized. This finding suggests that the current approaches, which focus on monitoring simple geometric features of the melt pool, may not be sufficient to ensure uniform

Table 4. Calculation of the pore detection accuracy rate and the false-positive rate for melt pool temperature distribution.

SOM model	Number of pores predicted accurately (Υ)	Number of false positives (Λ)	Pore detection accuracy rate (κ) (%)	False positive rate (%)
4 × 4	47	3	92.16	0.193
5 × 5	47	0	92.16	0.000
6 × 6	49	2	96.07	0.128
7 × 7	41	0	80.39	0.000
Actual number of pores		51		
Number of melt pools in thin wall (N)		1554		

Table 5. Calculation of the pore detection accuracy rate and the false-positive rate for the morphological model.

SOM model	Number of pores predicted accurately (Υ)	Number of false positives (Λ)	Pore detection accuracy rate (κ) (%)	False positive rate (%)
4 × 4	41	6	80.39	0.386
5 × 5	42	10	82.35	0.643
6 × 6	41	7	80.39	0.450
7 × 7	42	27	82.35	1.730
Actual number of pores		51		
Number of melt pools in thin wall (N)		1554		

Table 6. Confusion matrix for 4 × 4 SOM model using melt pool temperature distribution.

Actual	Predicted	
	Yes	No
Yes	TP = 47	FN = 3
No	FP = 1	TN = 1503

and stable melt pool profiles. The corresponding closed-loop control may not be able to capture process anomalies associated with more complex behaviors of variations.

For further clarification, we construct the confusion matrix. Subsequently, we calculate the measures that are required to calculate the F-Score measure. In the confusion matrix, TP, FN, FP, and TN express the number of true positive, false negative, false positive, and true negative, respectively. Furthermore, precision, recall, and F-Score account for the accuracy of each clustering model. In Table 6, the numerical results for the aforementioned measures are presented for the 4 × 4 SOM model using melt pool temperature distribution.

Three accuracy measures are calculated; i.e., precision, recall, and F-Score. These values can be expressed as

$$\begin{aligned}
 \text{Precision} &= \frac{TP}{TP + FP} = \frac{47}{48} = 97.91\% \\
 \text{Recall} &= \frac{TP}{TP + FN} = \frac{47}{50} = 94.00\% \\
 F &= \frac{2 \times (\text{Precision} \times \text{Recall})}{\text{Precision} + \text{Recall}} \\
 &= \frac{2 \times 0.9791 \times 0.94}{0.9791 + 0.94} = 95.92\%.
 \end{aligned}$$

Similarly, the F-Score for both melt pool morphological characteristics and temperature distribution of the melt pool can be calculated. Results show that the 6 × 6 SOM model provides the best F-Score value, which indicates high accuracy rate in terms of porosity prediction (see Table 7). This is consistent with the corresponding results in Section 5.3.

Table 7. Comparing the F-Score for clustering models using melt pool morphological characteristics (FMC) and temperature distribution (FTD).

SOM model	FMC	FTD
4 × 4	89.13	95.92
5 × 5	78.5	95.92
6 × 6	89.13	98.00
7 × 7	73.04	89.13

Note: Bold number refers to the best SOM model.

6. Conclusions

Inadvertent microstructure anomalies, such as porosity and mini-cracks, have detrimental effects on the mechanical properties of additively manufactured components. This hinders the wider adoption of AM technologies in strategic industrial sectors. We propose to predict porosity of as-built parts using the thermal distribution of melt pools during the build. Major findings of this study are summarized below:

1. Existing methods for porosity characterization mainly rely on post-manufacturing approaches, such as X-ray CT or ultrasonic scanning, which can be expensive and time-consuming. More important, post-manufacturing characterization does not allow for the detection and correction of porosity during the build, resulting in lower product quality. We propose an *in situ* monitoring tool for porosity prediction based on the similarity of melt pool thermal distributions. Our central hypothesis is that the similarities among melt pools are directly correlated to the formation of pores in as-built parts. Thus, the anomalies of melt pool thermal distribution can be used as a process signature that signals the anomalies in microstructure.
2. Capturing the similarity among melt pool images is challenging, due to the different size/shape of melt pools, missing data measurements during data acquisition, and the tremendous volume of data. To address these challenges, we develop a novel data processing procedure that is capable of converting ill-structured melt

pool image streams to continuous thermal distribution models with the identical function support. Once melt pool images are defined in the same domain, the clustering algorithm of an SOM is applied to group melt pool thermal distributions based on similarity, so that melt pools belonging to the same cluster share similar thermal distributions and tend to yield similar microstructures. On the other hand, melt pools from different clusters may exhibit different thermal behaviors. The dissimilarity between two clusters is characterized by their correlation. A cluster that has a low correlation with the others or includes only a small number of melt pools is considered to be an anomaly, which is predicted to result in porosity at the corresponding location.

3. We validate the proposed porosity prediction method by benchmarking against the X-ray CT characterization of a Ti-6Al-4V thin-wall build fabricated using a LENS system. The results show a prediction accuracy of over 96% and a false alarm rate of less than 0.02%. In other words, if the proposed prediction method is implemented during the build and the corresponding correction actions are taken before the subsequent layers are built, the porosity level of the as-built part can reduce to lower than 5% of the current level (without implementing our proposed *in situ* monitoring). This is expected to significantly enhance the durability and reliability of AM parts to a higher order of magnitude.
4. The comparative study with a previous work (Khanzadeh *et al.*, 2016) that focuses on the morphological features of melt pools (e.g., area, length, width, etc.) shows significant improvement in prediction accuracy. SOM clustering based on morphological features fails to form distinct clusters. This means that process monitoring solely based on such simple features is not sufficient for identification of anomalies. The thermal distribution within the melt pool should be taken into account.
5. Although the proposed *in situ* monitoring methodology is validated based on experimental data generated from a LENS process, the developed framework can serve as a “real-time X-ray CT” for other AM processes sharing similar energy–material interactions (e.g., Powder Bed Fusion, Electron Beam Melting, etc.), as long as the material is deposited via the solidification of a melt pool. By capturing the melt pool anomalies, our method can potential capture the microstructure anomalies in real time.

Our work provides a theoretical foundation for the online certification and qualification of AM products. Future work is needed to enable and facilitate real-time processing of thermal images, which is extremely challenging considering the large data volume and high data acquisition rate. Extra efforts are also needed to account for parts with complex geometries.

Although the thermo-physical dynamics for the DED process are not comprehensively investigated, this study is the first step in achieving this objective. The focus of this study is relating thermal history of the thin wall builds with microstructure. In future studies, the goal will be to investigate the effect of process parameters (e.g., powder feed rate, transverse speed, laser power, scanning pattern) and material properties on the

thermal history, which, in turn, affect the mechanical properties of the final product. Another possible extension of this work is to consider the re-melt phenomenon of AM fabrication.

Disclosure

The views and conclusions contained in this document are those of the authors and should not be interpreted as representing the official policies, either expressed or implied, of the Army Research Laboratory or the U.S. Government. The U.S. Government is authorized to reproduce and distribute reprints for Government purposes notwithstanding any copyright notation herein.

Funding

Research was sponsored by the Army Research Laboratory and was accomplished under Cooperative Agreement Number W911NF-15-2-0025.

Notes on contributors

Mojtaba Khanzadeh is a Ph.D. student in the Industrial and Systems Engineering Department at Mississippi State University and is pursuing another M.Sc. degree in the Statistics Department at Mississippi State University. He received his M.Sc. and B.Sc. in industrial and systems engineering from Sharif University of Technology in 2015 and 2013, respectively. Mojtaba Khanzadeh's research interests focus on using machine learning techniques for process characterization in Additive Manufacturing. He is a member of the Institute for Operations Research and the Management Sciences (INFORMS), the Institute of Industrial and Systems Engineers (IISE), and American Society of Mechanical Engineers (ASME).

Sudipta Chowdhury received his B.Sc. in industrial and systems engineering from Shahjalal University of Science and Technology in 2014. He is currently a graduate student in the Department of Industrial and Systems Engineering at Mississippi State University.

Mark A. Tschopp is the Regional Lead for ARL Central at the U.S. Army Research Laboratory, having previously been a materials engineer, team leader, and branch chief in the Weapons and Materials Research Directorate. His primary research interests lie in integrating computational and experimental techniques to design materials for lightweight vehicle applications, soldier protection systems, and lethality applications in support of the warfighter and the mission of the U.S. Army. He was elected as an ASME Fellow in 2017.

Haley R. Doude is a research engineer at the Center for Advanced Vehicular Systems at Mississippi State University (MSU). She received a competitive NASA fellowship to fund her doctoral degree research in friction stir welding. She earned her Ph.D. in mechanical engineering from MSU in 2014 and her bachelor's degree in biological engineering from MSU in 2006. Her background is in material science with a focus on design and processing of metals. Current projects include steel alloy design and material science studies related to additive manufacturing. Sponsors for her research include DoD, NASA, and industrial partners.

Mohammad Marufuzzaman received his Ph.D. in industrial and systems engineering from Mississippi State University in 2014. He then joined the department as an assistant professor in August 2015. His main areas of interest are in supply chain optimization with an application in renewable energy, stochastic programming, decomposition methods, solving large-scale network flow problems, and supply chain risk management. His publications have appeared in journals such as *Transportation Science*, *Annals of Operations Research*, *Computers and Operations Research*, *Transportation Research Part E*, *International Journal of Production Economics*, and several conference proceedings. He is a member of INFORMS and IIE.

Linkan Bian is an assistant professor in the Industrial and Systems Engineering Department at Mississippi State University. He received his Ph.D. in industrial and systems engineering from Georgia Institute of Technology in 2013. He also holds a dual M.S. degree in statistics and mathematics

from Michigan State University and a B.S. degree in applied mathematics from Beijing University. His research interests focus on the combination of advanced statistics and stochastic methods for system modeling, diagnosis, and prognosis. Applications of his research include advanced manufacturing systems and supply chains. He is currently participating in a DoD project focusing on uncertainty quantification and process optimization in Additive Manufacturing processes. His research is also funded by FedEx Express. His publications have appeared in journals such as *Institute of Industrial Engineers (IIE) Transactions*, *Statistical Analysis and Data Mining*, *Naval Research Logistics*, and several conference proceedings. He is a member of the Institute for Operations Research and the Management Sciences (INFORMS) and the Institute of Industrial and Systems Engineers (IISE).

References

- Abraham, O., Piwakowski, B., Villain, G. and Durand, O. (2012) Non-contact, automated surface wave measurements for the mechanical characterisation of concrete. *Construction and Building Materials*, **37**, 904–915.
- Ahn, I.H., Moon, S.K., Hwang, J. and Bi, G. (2017) Characteristic length of the solidified melt pool in selective laser melting process. *Rapid Prototyping Journal*, **23**(2), 370–381.
- Bi, G., Gasser, A., Wissenbach, K., Drenker, A. and Poprawe, R. (2006) Characterization of the process control for the direct laser metallic powder deposition. *Surface and Coatings Technology*, **201**(6), 2676–2683.
- Birnbaum, A., Aggarangsi, P. and Beuth, J.L. (2003) Process scaling and transient melt pool size control in laser-based additive manufacturing processes, in *Proceedings of Solid Freeform Fabrication Symposium*, Solid Freeform Fabrication Proceedings, Austin, TX, pp. 328–339.
- Boddu, M.R., Landers, R.G. and Liou, F.W. (2001) Control of laser cladding for rapid prototyping: A review, in *Proceedings of the Solid Freeform Fabrication Symposium*, Solid Freeform Fabrication Proceedings, Austin, TX, pp. 6–8.
- Cai, X., Malcolm, A.A., Wong, B.S. and Zheng, F. (2015) Measurement and characterization of porosity in aluminium selective laser melting parts using X-ray CT. *Virtual and Physical Prototyping*, **10**(4), 195–206.
- Chandrasekhar, N., Vasudevan, M., Bhaduri, A.K. and Jayakumar, T. (2015) Intelligent modeling for estimating weld bead width and depth of penetration from infra-red thermal images of the weld pool. *Journal of Intelligent Manufacturing*, **26**(1), 59–71.
- Chowdhury, S., Khanzadeh, M., Akula, R., Zhang, F., Zhang, S., Medal, H., Marufuzzaman, M. and Bian, L. (2017) Botnet detection using graph-based feature clustering. *Journal of Big Data*, **4**(14). doi:10.1186/s40537-017-0074-7
- Clijsters, S., Craeghs, T., Buls, S., Kempen, K. and Kruth, J.P. (2014) In situ quality control of the selective laser melting process using a high-speed, real-time melt pool monitoring system. *The International Journal of Advanced Manufacturing Technology*, **75**(5–8), 1089–1101.
- Cunningham, R., Narra, S.P., Montgomery, C., Beuth, J. and Rollett, A.D. (2017) Synchrotron-based X-ray microtomography characterization of the effect of processing variables on porosity formation in laser powder-bed additive manufacturing of Ti-6Al-4V. *The Journal of The Minerals, Metals and Materials Society*, **69**(3), 479–484.
- De Chiffre, L., Carmignato, S., Kruth, J.P., Schmitt, R. and Weckenmann, A. (2014) Industrial applications of computed tomography. *CIRP Annals-Manufacturing Technology*, **63**(2), 655–677.
- Dilip, J.J.S., Zhang, S., Teng, C., Zeng, K., Robinson, C., Pal, D. and Stucker, B. (2017) Influence of processing parameters on the evolution of melt pool, porosity, and microstructures in Ti-6Al-4V alloy parts fabricated by selective laser melting. *Progress in Additive Manufacturing*, **2**(3), 157–167.
- Ding, Y., Warton, J. and Kovacevic, R. (2016) Development of sensing and control system for robotized laser-based direct metal addition system. *Additive Manufacturing*, **10**, 24–35.
- Doumanidis, C. and Kwak, Y. (2001) Geometry modeling and control by infrared and laser sensing in thermal manufacturing with material deposition. *Transactions-American Society of Mechanical Engineers Journal of Manufacturing Science and Engineering*, **123**(1), 45–52.
- Eren, E., Kurama, S. and Solodov, I. (2012) Characterization of porosity and defect imaging in ceramic tile using ultrasonic inspections. *Ceramics International*, **38**(3), 2456–2451.
- Fan, K., Chen, S., Chen, J. and Liao, W. (2010) Development of auto defect classification system on porosity powder metallurgy products. *NDT and E International*, **43**(6), 451–460.
- Fritzke, B. (1995) Growing grid: A self-organizing network with constant neighborhood range and adaptation strength. *Neural Processing Letters*, **2**(5), 9–13.
- Garnier, V., Piwakowski, B., Abraham, O., Villain, G., Payan, C. and Chaix, J.F. (2013) Acoustic techniques for concrete evaluation: Improvements, comparisons and consistency. *Construction and Building Materials*, **43**, 598–613.
- Gáspár, C. (1999) Multigrid technique for biharmonic interpolation with application to dual and multiple reciprocity method. *Numerical Algorithms*, **21**(1–4), 165–183.
- Gockel, J., Beuth, J. and Tamingier, K. (2014) Integrated control of solidification microstructure and melt pool dimensions in electron beam wire feed additive manufacturing of Ti-6Al-4V. *Additive Manufacturing*, **1**, 119–126.
- Goueygou, M., Lafhaj, Z. and Soltani, F. (2009) Assessment of porosity of mortar using ultrasonic Rayleigh waves. *NDT and E International*, **42**, 353–360.
- Hale, D. (2009) Image-guided blended neighbor interpolation. CWP Report, 634.
- Heigel, J.C., Michaleris, P. and Reutzel, E.W. (2015) Thermo-mechanical model development and validation of directed energy deposition additive manufacturing of Ti-6Al-4V. *Additive Manufacturing*, **5**, 9–19.
- Hsieh, J. (2003) *Computed Tomography: Principles, Design, Artifacts, and Recent Advances*, SPIE Press, Bellingham, WA.
- Hu, D. and Kovacevic, R. (2003) Modelling and measuring the thermal behaviour of the molten pool in closed-loop controlled laser-based additive manufacturing. *Proceedings of the Institution of Mechanical Engineers, Part B: Journal of Engineering Manufacture*, **217**(4), 441–452.
- Hua, T., Jing, C., Xin, L., Fengying, Z. and Weidong, H. (2008) Research on molten pool temperature in the process of laser rapid forming. *Journal of Materials Processing Technology*, **198**(1), 454–462.
- Hunt, J.D. (1984) Steady state columnar and equiaxed growth of dendrites and eutectic. *Materials Science and Engineering*, **65**(1), 75–83.
- Jafari-Marandi, R. and Keramati, A. (2014) Webpage clustering—Taking the zero step: a case study of an Iranian website. *Journal of Web Engineering*, **13**(3–4), 333–360.
- Khairallah, S.A., Anderson, A.T., Rubenchik, A. and King, W.E. (2016) Laser powder-bed fusion additive manufacturing: Physics of complex melt flow and formation mechanisms of pores, spatter, and denudation zones. *Acta Materialia*, **108**, 36–45.
- Khanzadeh, M., Bian, L., Shamsaei, N. and Thompson, S.M. (2016) Porosity detection of laser based additive manufacturing using melt pool morphology clustering, in *Solid Freeform Fabrication: Proceedings of the 27th Annual International Solid Fabrication Symposium—An Additive Manufacturing Conference*, Solid Freeform Fabrication, Austin, TX, pp. 1487–1494.
- Kim, J.D. and Peng, Y. (2000) Melt pool shape and dilution of laser cladding with wire feeding. *Journal of Materials Processing Technology*, **104**(3), 284–293.
- Kobryn, P.A. and Semiatin, S.L. (2001) The laser additive manufacture of Ti-6Al-4V. *Journal of the Minerals, Metals and Materials Society*, **53**(9), 40–42.
- Kobryn, P.A. and Semiatin, S.L. (2003) Microstructure and texture evolution during solidification processing of Ti-6Al-4V. *Journal of Materials Processing Technology*, **135**(2), 330–339.
- Kowaluk, T. and Woźniak, A. (2012) Study of porosity measurement using the computer tomograph. *Pomiary Automatyka Robotyka*, **16**(12), 82–86.
- Kruth, J.P., Bartscher, M., Carmignato, S. and Schmitt, R. (2011) Computed tomography for dimensional metrology. *CIRP Annals-Manufacturing Technology*, **60**(2), 821–842.
- Kruth, J.-P. (2017) On-line monitoring and process control in selective laser melting and laser cutting. In M. Geiger et al. (Eds.), *Proceedings of the 5th Lane Conference*, Laser Assisted Net Shape Engineering 2007, pp. 23–37.

- Lafhaj, Z., Goueygou, M., Djerbi, A. and Kaczmarek, M. (2006) Correlation between porosity, permeability and ultrasonic parameters of mortar with variable water/cement ratio and water content. *Cement and Concrete Research*, **36**(4), 625–633.
- Li, S., Xiao, H., Liu, K., Xiao, W., Li, Y., Han, X., Mazumder, J. and Song, L. (2017) Melt-pool motion, temperature variation and dendritic morphology of Inconel 718 during pulsed- and continuous-wave laser additive manufacturing: A comparative study. *Materials and Design*, **119**, 351–360.
- Marshall, G.J., Thompson, S.M. and Shamsaei, N. (2016) Data indicating temperature response of Ti-6Al-4V thin-walled structure during its additive manufacture via laser engineered net shaping. *Data in Brief*, **7**, 697–703.
- Meola, C. and Toscano, C. (2014) Flash thermography to evaluate porosity in carbon fiber reinforced polymer (CFRPs). *Materials*, **7**(3), 1483–1501.
- Merényi, E., Mendenhall, M.J. and Patrick, O. (2016) Advances in self-organizing maps and learning vector quantization, in *Proceedings of the 11th International Workshop WSOM 2016, Workshop on Self-Organizing Maps*, Houston, TX, USA.
- Mireles, J., Ridwan, S., Morton, P.A., Hinojos, A. and Wicker, R.B. (2015) Analysis and correction of defects within parts fabricated using powder bed fusion technology. *Surface Topography: Metrology and Properties*, **3**(3), 1–8.
- Nassar, A.R., Spurgeon, T.J. and Reutzel, E.W. (2014) Sensing defects during directed-energy additive manufacturing of metal parts using optical emissions spectroscopy, in *Proceedings of the Solid Freeform Fabrication Symposium*, Solid Freeform Fabrication Proceedings, Austin, TX, 278–287.
- Patel, R. and Giri, V.K. (2016) Analysis and interpretation of bearing vibration data using principal component analysis and self-organizing map. *International Journal of Advanced Design and Manufacturing Technology*, **9**(1), 111–117.
- Picasso, M. and Hoadley, A.F.A. (1994) Finite element simulation of laser surface treatments including convection in the melt pool. *International Journal of Numerical Methods for Heat and Fluid Flow*, **4**(1), 61–83.
- Pinkerton, A. and Lin, L. (2004) Modelling the geometry of a moving laser melt pool and deposition track via energy and mass balances. *Journal of Physics D: Applied Physics*, **37**(14), 1885–1895.
- Pratiwi, D. (2012) The use of self organizing map method and feature selection in image database classification system. ArXiv preprint arXiv:1206.0104.
- Qi, H., Mazumder, J. and Ki, H. (2006) Numerical simulation of heat transfer and fluid flow in coaxial laser cladding process for direct metal deposition. *Journal of Applied Physics*, **100**(2), 1–11.
- Sandwell, D.T. (1987) Biharmonic spline interpolation of GEOS-3 and SEASAT altimeter data. *Geophysical Research Letters*, **14**(2), 139–142.
- Schwerdtfeger, J., Robert, S.F. and Körner, C. (2012) In situ flaw detection by IR-imaging during electron beam melting. *Rapid Prototyping Journal*, **18**(4), 259–263.
- Seifi, M., Salem, A., Beuth, J., Harrysson, O. and Lewandowski, J.J. (2016) Overview of materials qualification needs for metal additive manufacturing. *Journal of Materials*, **68**(3), 747–764.
- Shamsaei, N., Yadollahi, A., Bian, L. and Thompson, S.M. (2015) An overview of direct laser deposition for additive manufacturing; Part II: Mechanical behavior, process parameter optimization and control. *Additive Manufacturing*, **8**, 12–35.
- Shiomi, M., Yoshidome, A., Abe, F. and Osakada, K. (1999) Finite element analysis of melting and solidifying processes in laser rapid prototyping of metallic powders. *International Journal of Machine Tools and Manufacture*, **39**(2), 237–252.
- Siddique, S., Imran, M., Rauer, M., Kaloudis, M., Wycisk, E., Emmelmann, C. and Walther, F. (2015) Computed tomography for characterization of fatigue performance of selective laser melted parts. *Materials and Design*, **83**, 661–669.
- Soltani, F., Goueygou, M., Lafhaj, Z., Piwakowski, B. (2013) Relationship between ultrasonic Rayleigh wave propagation and capillary porosity in cement paste with variable water content. *NDT and E International*, **54**, 75–83.
- Song, L., Bagavath-Singh, V., Dutta, B. and Mazumder, J. (2012) Control of melt pool temperature and deposition height during direct metal deposition process. *The International Journal of Advanced Manufacturing Technology*, **58**(1-4), 247–256.
- Soylomez, E., Beuth, J. and Taminger, K. (2010) Controlling melt pool dimensions over a wide range of material deposition rates in electron beam additive manufacturing, in *Proceedings of 21st Solid Freeform Fabrication Symposium*, Solid Freeform Fabrication Proceedings, Austin, TX, pp. 9–11.
- Tajeripour, F. and Fekri-Ershad, S.H. (2012) Porosity detection by using improved local binary pattern, in *Proceedings of the 11th WSEAS International Conference on Signal Processing, Robotics and Automation* (isptra '12), Cambridge, UK.
- Tang, L. and Landers, R.G. (2010) Melt pool temperature control for laser metal deposition processes. Part I: Online temperature control. *Journal of Manufacturing Science and Engineering*, **132**(1), 1–9.
- Tang, L., Sparks, T.E., Ruan, J., Landers, R.G. and Liou, F.W. (2009) Online melt pool temperature control for laser metal deposition processes. Report, in *Proceedings of the 3rd Annual ISC Research Symposium*, Missouri University of Science and Technology, Rolla, MO.
- Tang, M., Pistorius, P.C. and Beuth, J.L. (2017) Prediction of lack-of-fusion porosity for powder bed fusion. *Additive Manufacturing*, **14**, 39–48.
- Thompson, S.M., Bian, L., Shamsaei, N. and Yadollahi, A. (2015) An overview of direct laser deposition for additive manufacturing; Part I: Transport phenomena, modeling and diagnostics. *Additive Manufacturing*, **8**, 36–62.
- Vetter, P.A., Engel, T. and Fontaine, J. (1994) Laser cladding: The relevant parameters for process control. *Proceedings of the Society of Photo-Optical Instrumentation Engineers*, **2207**, 452–462.
- Wang, Q., Li, J., Gouge, M., Nassar, A.R. and Michaleris, P.P. (2017) Physics-based multivariable modeling and feedback linearization control of melt-pool geometry and temperature in directed energy deposition. *Journal of Manufacturing Science and Engineering*, **139**(2), p. 021013.
- Wells, J.M. (2007) Quantitative XCT evaluation of porosity in an aluminum alloy casting, in *Shape Casting: Second International Symposium*, Taylor and Francis, London, UK, pp. 1–43.
- Wohlers, T. (2016) Wohlers report 2016. Wohlers Associates, Inc.

Appendix

Table A1. Cluster correlation and percentage of melt pool in each cluster in 5×5 SOM model with model of melt pool thermal profile.

Centroid ID	C15	C55	C45	C11	C25	C35	C14	C54	C44	C12	C51	C21	C34
Median	0.42	0.69	0.73	0.79	0.86	0.88	0.90	0.91	0.94	0.95	0.95	0.95	0.96
Melt pool ratio	0.06	0.77	0.58	0.06	0.45	1.09	0.38	3.64	7.03	0.51	3.26	1.21	4.67
Centroid ID	C53	C41	C23	C24	C31	C42	C22	C13	C43	C52	C32	C33	
Median	0.97	0.97	0.97	0.97	0.97	0.98	0.98	0.98	0.98	0.98	0.98	0.98	
Melt pool ratio	6.97	7.03	3.20	2.75	5.88	9.91	4.22	3.20	10.42	5.43	8.57	8.06	

Note: Bold numbers account for the clusters and are chosen by decision rules and hypothesis.

Table A2. Cluster correlation and percentage of melt pool in each cluster in 6×6 SOM model with model of melt pool thermal profile.

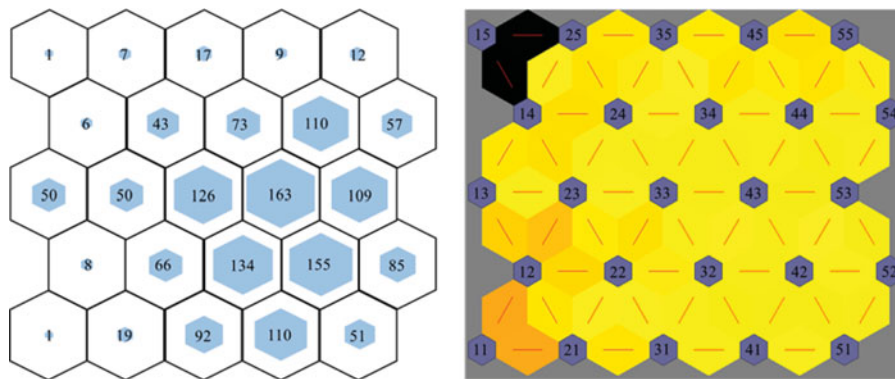
Centroid ID	C16	C56	C66	C11	C26	C36	C15	C46	C65	C21	C55	C12	C25
Median	0.40	0.69	0.71	0.81	0.87	0.87	0.88	0.91	0.91	0.95	0.95	0.95	0.96
Melt pool ratio	0.06	0.45	0.77	0.06	0.51	0.64	0.77	1.85	2.30	0.77	4.80	0.51	1.60
Centroid ID	C35	C45	C64	C61	C63	C54	C31	C41	C33	C14	C22	C44	C51
Median	0.96	0.96	0.96	0.97	0.97	0.97	0.97	0.97	0.97	0.97	0.97	0.98	0.98
Melt pool ratio	2.30	4.09	4.16	1.92	3.32	5.69	2.43	2.30	0.70	1.66	1.98	5.12	3.58
Centroid ID	C24	C53	C32	C13	C62	C23	C42	C34	C43	C52			
Median	0.98	0.98	0.98	0.98	0.98	0.98	0.98	0.98	0.98	0.98			
Melt pool ratio	4.28	6.33	5.37	2.11	4.16	4.35	2.81	6.14	4.48	4.99			

Note: Bold numbers account for the clusters and are chosen by decision rules and hypothesis.

Table A3. Cluster correlation and percentage of melt pool in each cluster in 7×7 SOM model with model of melt pool thermal profile.

Centroid ID	C17	C67	C77	C11	C47	C37	C66	C57	C27	C76	C21	C22	C12
Median	0.40	0.68	0.71	0.81	0.85	0.87	0.90	0.90	0.91	0.92	0.94	0.94	0.95
Melt pool ratio	0.06	0.45	0.77	0.06	0.83	0.45	1.41	0.19	0.38	2.37	0.77	0.45	0.38
Centroid ID	C46	C56	C64	C36	C41	C61	C74	C16	C63	C73	C25	C75	C26
Median	0.96	0.96	0.96	0.96	0.97	0.97	0.97	0.97	0.97	0.97	0.97	0.97	0.97
Melt pool ratio	1.98	2.11	4.48	1.73	1.15	1.60	3.64	0.96	1.21	2.88	1.47	2.56	0.70
Centroid ID	C31	C13	C23	C55	C51	C54	C72	C45	C32	C14	C65	C15	C33
Median	0.97	0.97	0.98	0.98	0.98	0.98	0.98	0.98	0.98	0.98	0.98	0.98	0.98
Melt pool ratio	2.69	1.53	2.62	2.05	2.30	4.54	1.73	3.58	4.28	2.17	3.52	1.09	3.84
Centroid ID	C52	C35	C44	C24	C53	C71	C43	C34	C62	C42			
Median	0.98	0.98	0.98	0.98	0.98	0.98	0.99	0.99	0.99	0.99			
Melt pool ratio	3.39	1.98	2.17	3.26	2.37	1.79	2.05	3.39	4.41	3.58			

Note: Bold numbers account for the clusters and are chosen by decision rules and hypothesis.

**Figure A1.** SOM for 5×5 model with melt pool thermal profile.

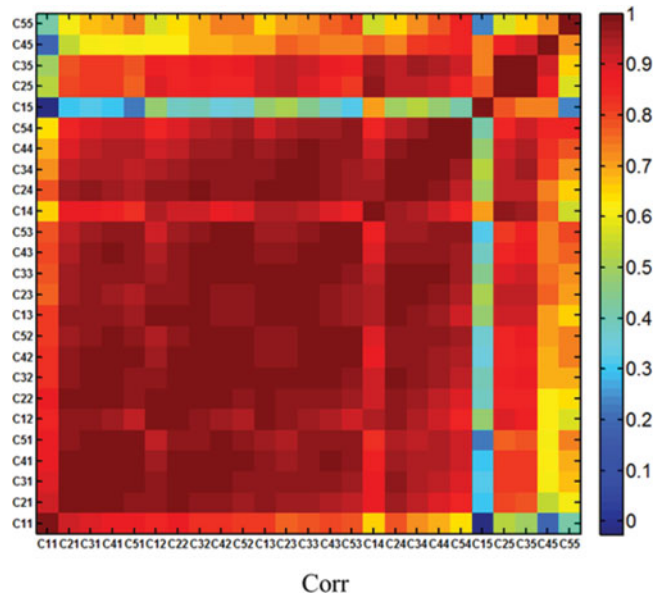


Figure A2. Correlation matrix (Cor) showing how pores were identified with melt pool thermal profile for the 25 clusters (Corr) of the 5×5 SOM map.

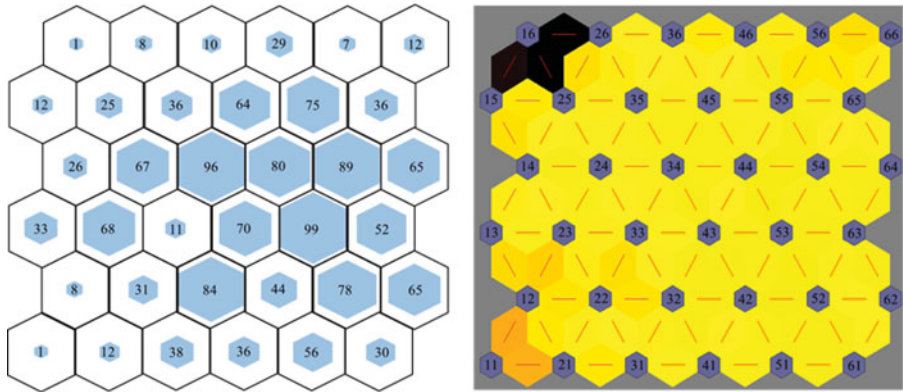


Figure A3. SOM for 6×6 model with melt pool thermal profile.

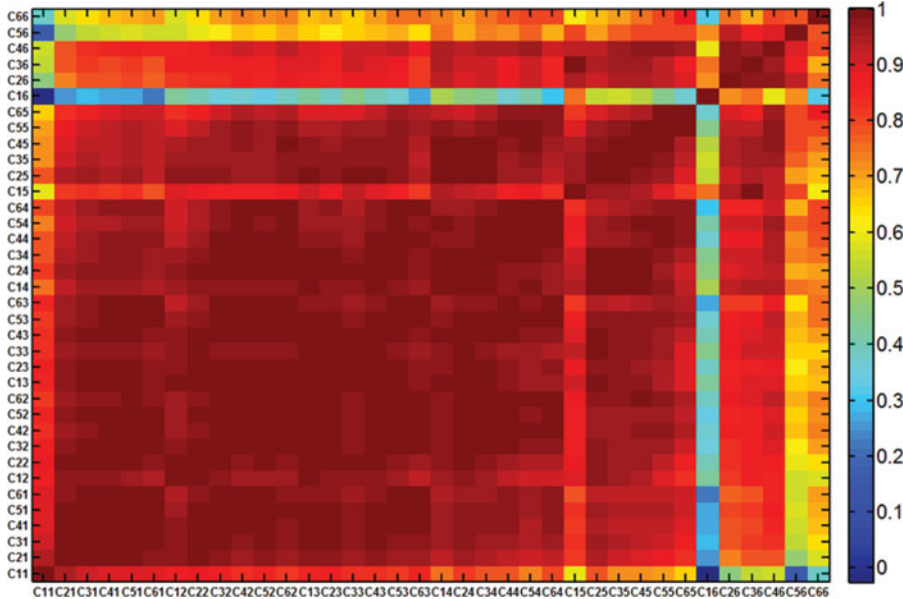


Figure A4. Correlation matrix (Cor) showing how pores were identified with melt pool thermal profile for the 36 clusters (Corr) of the 6×6 SOM map.

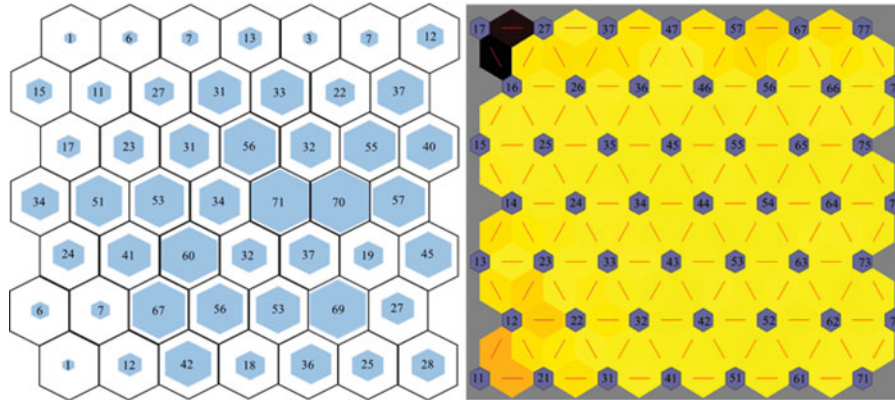


Figure A5. SOM for 7×7 model with melt pool thermal profile.

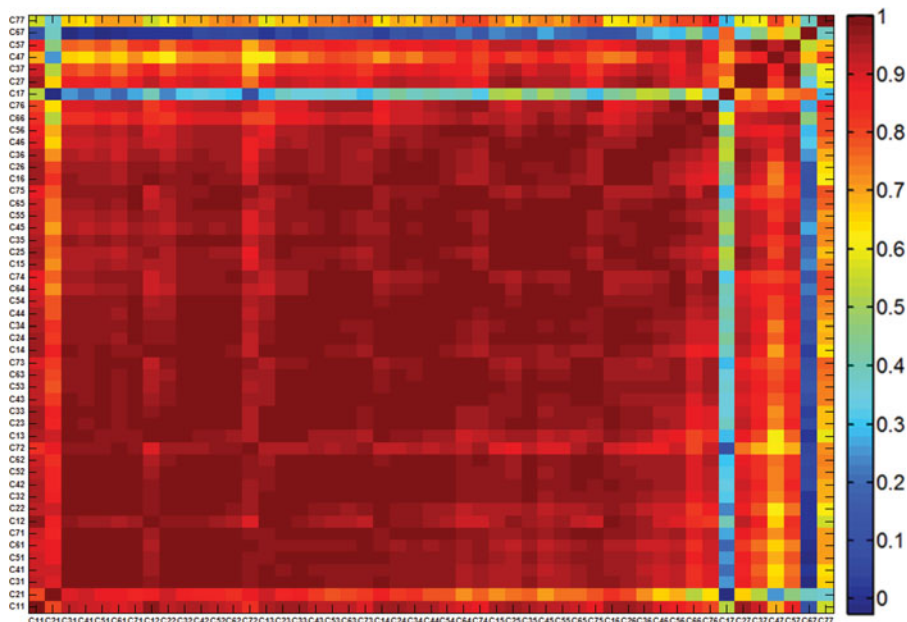


Figure A6. Correlation matrix (Cor) showing how pores were identified with melt pool thermal profile for the 49 clusters (Corr) of the 7×7 SOM map.